Employing MS-UNets Networks for Multiscale 3-D Gravity Data Inversion: A Case Study in the Nordkapp Basin, Barents Sea

Rui Wang, Yaming Ding, Zhengwei Xu, Michael S. Zhdanov, *Member, IEEE*, Minghao Xian, Yu Zhang, Jun Li, Chao Jiang, and Ziqing Guo

Abstract— Salt domes are very important in hydrocarbon exploration and identification of potential drilling hazards. While seismic data are indispensable for detailed subsurface imaging, especially in delineating the geometry and properties of salt bodies and their boundaries, gravity inversion provides an additional layer of data by exploiting the density differential. However, traditional methodologies for tackling this problem are complicated by the ill-posedness of the inverse problems. The alternative approach to gravity image is based on machine learning (ML) algorithms. Despite the appealing attributes of convolutional neural networks (CNNs), they are not exempt from limitations, including diminished precision in pinpointing geological features, complications in managing the varying scales of geological structures, and inefficiencies in processing voluminous, high-dimensional data. These deficits can be mitigated by the proposed multiscale functional multiscale UNets (MS-UNets) network, which, through integration with squeeze-and-excitation (S-E) and strip pooling (S-P) modules, are designed to enhance the capture of detailed information about salt domes. These networks were subjected to rigorous testing using both synthetic and real gravity data, showcasing their robustness across diverse scenarios. This testing highlighted their significant potential for applications in geophysical data interpretation, structural modeling, and inversion processes.

Index Terms— 3-D inversion, gravity and gravity gradiometry, multiscale UNets (MS-UNets).

I. INTRODUCTION

SALT domes are large geological structures formed by the upward movement of salt in the Earth's crust. They are often associated with oil and gas reservoirs, as the salt can create traps that hold hydrocarbons in place. These traps can take many forms, such as anticlines, fault blocks, and stratigraphic traps, and understanding the geometry and structure of the salt dome can help identify the type of trap present. Studying salt dome morphology can also help identify potential hazards associated with drilling in salt domes, such as the risk of drilling into overpressured zones or encountering subsurface salt cavities.

Seismic surveys are particularly useful, as they can provide detailed information about the structure of the subsurface, including the thickness and depth of the salt layer, the shape and orientation of the dome, and the presence of any faults or fractures. Researchers analyze 3-D seismic datasets to study the internal architecture of the sea-bottom salt domes, utilizing seismic attribute analysis and stratigraphic interpretation to identify their layers and structures, including potential hydrocarbon traps [1], [2], [3], [4]. A methodology for precisely imaging the subsurface geometry of salt domes has been developed, which involves utilizing a combination of full-waveform inversion and reverse-time migration techniques [5], [6], [7].

Recently, researchers utilized seismic technology and a combination of techniques, including prestack depth migration and reverse-time migration [8], [9], [10], [11], rock physics modeling [12], [13], seismic inversion [14], [15], and structural interpretation, to produce high-resolution images of the internal structure of salt domes, map their potential hydrocarbon traps, and investigate the subsurface structure of salt domes. Despite the detailed insights offered by seismic technology, there are inherent challenges in interpreting salt-sediment interfaces, particularly in complex geological environments.

In such scenarios, gravity inversion emerges as a complementary technique. It leverages the distinct density contrasts between salt structures and surrounding formations, offering a different modality of subsurface analysis that can validate or refine seismic interpretations. Henke et al. [16] utilized magnetotellurics (MT), integrated with seismic and gravity data, to enhance the imaging of the Wedehof salt dome in the Northern German Basin, reducing exploration drilling risks. A new, easily applicable 2-D semiinversion gravitational technique has been introduced, utilizing Bouguer gravity anomaly

data to separate Bouguer anomaly into its corresponding rock formations, estimate and trace sedimentary formation depths relative to the underlying geometry of Humble Salt Dome, USA [17]. Ghari et al. [18] investigate the dome-shaped salt unit in the Qarah-Aghaje area, Iran, using an integrated approach that combines 3-D inversion models from gravity and magnetic data, geological, and well observations, applying a weighted damped minimum length solution. Several researchers proposed a multiphysics approach to study the salt domes [19], [20], [21], [22], [23], [24], [25], [26], [27], [28].

Still, salt-dome interpretation based on seismic and other types of geophysical data is a critical but time-consuming and human-intensive process that can consume significant resources during the model-building workflows of large 3-D surveys, often spanning several weeks or months, which can be further complicated by iterative sediment and salt-flooding techniques requiring multiple rounds of salt interpretation.

The infusion of prior geological information to unravel inverse problems via the lens of machine learning (ML) has seen growing interest. Numerous recent studies propose deploying unsupervised ML algorithms to tackle inverse gravity problems [29], [30], [31], [32]. Despite this, unsupervised learning necessitates a degree of geological knowledge to verify the output. Contrarily, supervised ML techniques, informed by a priori geological information, can extrapolate geological models from new and unseen data that extends beyond the range of the training data. Prevalent classification and regression algorithms, including linear classifiers [33], [34], support vector machines [35], decision trees [36], and random forests [37], [38], have been harnessed to grapple with the ill-posed problems inherent to geophysical inverse situations. Additionally, linear regression [21], logistic regression [39], and polynomial regression [40], [41] have proven effective in restoring subsurface physical characteristics. However, despite its efficacy, traditional supervised learning methods, distinct from deep learning (DL) approaches, often face limitations in handling complex tasks, and the computational demands of their training processes, while significant, are generally less than those required for DL models.

DL, while often associated with supervised learning, is a versatile approach that is also applicable in unsupervised learning and reinforcement learning contexts. It employs a neural network to emulate the analytical learning mechanism of the human brain, thereby aiding in the interpretation of geoscience data through the comprehension of data-model property relationships [42], [43]. Given its superior capabilities in feature learning and information extraction, DL presents a potent supplement to traditional geophysical inversion. For instance, alterations in density values, 3-D structures, and the distribution of anomalous bodies beneath the surface precipitate changes in 2-D gravity observational data at the surface. Convolutional neural networks (CNNs) utilize end-to-end learning to discern and map the relationships between 2-D gravity data and their associated 3-D density models [44], [45], [46], [47], [48]. However, the limitations of traditional CNNs are particularly evident in scenarios where high-resolution spatial information is paramount. For instance, in the case of gravity inversion, the loss of fine-grained details can lead to

inaccurate localization of subsurface features, such as faults and fractures. This is further compounded when dealing with geological structures that vary widely in scale, from vast sedimentary layers to narrow mineral veins, which CNNs struggle to simultaneously resolve. Moreover, the high dimensionality of geophysical data often necessitates a prohibitive amount of labeled data for training, which is not always feasible.

UNets, initially proposed by Ronneberger et al. [49], addresses these limitations with its unique architecture, thus potentially offering significant advantages in the context of gravity inversion in geophysical exploration. Recent studies [50], [51], [52], [53] have highlighted the potential of UNets in addressing the multifaceted challenges of gravity inversion. However, these conventional networks may inadvertently homogenize critical features, such as the subtle gradations in density that delineate the edges of salt domes. For example, the homogenization issue becomes apparent when UNets fail to differentiate between the dome cap rock and surrounding sediments, leading to a blurred representation of the geometry of salt dome [54], [55], [56], [57].

The quest for accurate subsurface imaging has led to the adoption of various ML algorithms, with recent research advocating for UNets to tackle the complexities of gravity inversion for delineating salt dome geometries [53], [58], [59], [60]. Despite their potential, conventional UNets often fall short in capturing the full spectrum of geological intricacies, sometimes over-simplifying or overlooking critical details. Hence, to better capture the complex interdependencies between different geological structures, the squeeze-and-excitation (S-E) module is introduced and architected with the objective of enhancing the efficacy of UNets in identifying and utilizing the intricate interdependencies across varying channels. This design aims to bolster UNets' performance in complex tasks such as geophysical inversion. Within the geophysics community, efforts are being made toward integrating UNet and S-E modules to generate high-precision imaging of salt domes [61], [62]. Meanwhile, the introduction of the strip pooling (S-P) module in the DL algorithm helps overcome the difficulties associated with accurately detecting and interpreting intricate, strip-like formations within data, which is important for subsurface modeling. However, no published studies are exploring the application of the S-P module for the recovery of salt domes through geophysical data analysis.

This article proposes a novel inversion networks model based on the UNet encoder-decoder architecture, designed to establish a neural network framework that transitions from surface gravity response data to the subsurface semi-infinite geological model. Subsequently, a multiscale UNet (MS-UNet) architecture inspired by the amalgamation of S-P and S-E modules is formulated to tackle the variable scale data input problem, enhancing the delineation of the salt dome boundary. Finally, the network mode's capability to reconstruct the density distribution in response to acquired gravity data is validated by analyzing synthetic and real gravity data collected in Nordkapp Basin, Barents Sea, which tests the network robustness and accuracy.

II. Inversion Methodology Based on MS-UNet Network

A. Generation of Training Sets

In order to obtain accurate density, depth, size, and other attributes of geological targets, it is necessary to construct a comprehensive training sample set comprising diverse geological body shapes. Theoretically, the training sample set should simulate the most probable distribution of the geological bodies and their corresponding gravity anomalies. Therefore, selecting appropriate methods and parameters for generating a training sample set with optimal performance, universality, and the ability to mimic real data distribution is a significant challenge.

We now delve into the practical implementation of these concepts, focusing on the construction of training density model sets first.

1) Training Density Models Sets: In the implementation of gravity data forward modeling, we define the lower half-space of the observation area as a $4000 \times 4000 \times 4000$ m volume. This space is initially divided into $20 \times 20 \times 20$ rectangular prisms, each measuring $200 \times 200 \times 200$ m. A total of 1681 (41×14) observation points are strategically placed above this half-space on a measurement plane. The density values for these models are randomly assigned as either 0.5 or 1 g/cm^3 to create a realistic underground simulation. We employ three distinct model generation methods—single block, isolated blocks, and contact assembly blocks—to simulate a wide range of geological bodies with varying density anomalies. To mitigate edge effects, our model deliberately excludes two cells (400 m in total) along the grid line's edge. Fig. 1 illustrates a flowchart of this training set generation process. Ultimately, gravitational anomaly values at each point within the measurement network space are calculated using a forward modeling formula.

This process generates either a single or combined random model with a total of 14 200 sets, where one set includes one density model and a corresponding calculated gravity anomaly. The single model represents a regular-shaped cube with randomly obtained positions and sizes [see Fig. 2(a) and (b)]. The combined models are composed of single models. There are two types of combined models. The first type is called "*separated combined models*" [see Fig. 2(c)]. These models consist of two single models generated independently. The second type is called "*contact assembly models*." It is generated by combining multiple individual models in a manner that imposes certain constraints on them. In contrast to the separated models, the contact assembly models are generated from the randomly selected single models under the constraints derived from the initially selected set of models.

2) Training Gravity Anomaly Datasets: In order to simulate the gravity anomaly datasets, g_z, of the designed corresponding subsurface geologic body models aforementioned above, we give the gravity forward modeling formula [63] as

$$\frac{\partial V}{\partial z} = g_z = G \iiint_v \frac{\rho(\zeta - z)d\xi d\eta d\zeta}{\left[(\xi - x)^2 + (\eta - y)^2 + (\zeta - z)^2\right]^{3/2}}$$
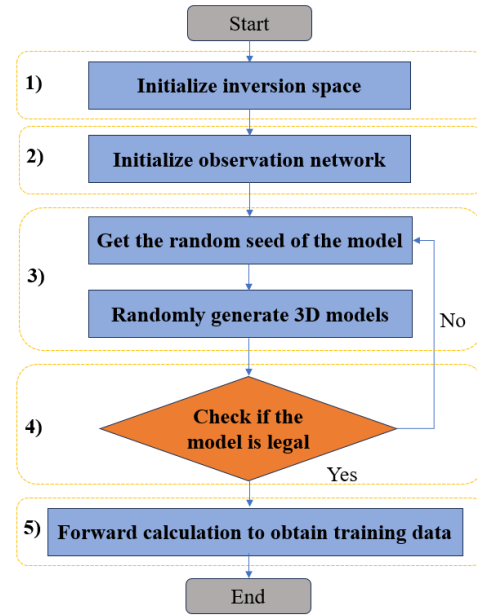
(1)

Fig. 1.   Workflow of the training set generation. (1) Initialize inversion space with $4000 \times 4000 \times 4000$ m is subdivided into 8000 rectangular prisms. (2) A total of 1681 observed points are placed on a measurement plane. (3) Three type of density models (single model, isolated models, and contact assembly model) are randomly generated. (4) Generated density models undergo a thorough legality check by verifying that the anomalies fall within the boundaries of the inversion space and ensuring the model excludes two cells at the edges of each grid line. (5) Gravitational anomaly values at each observed point are calculated using the forward modeling formula.
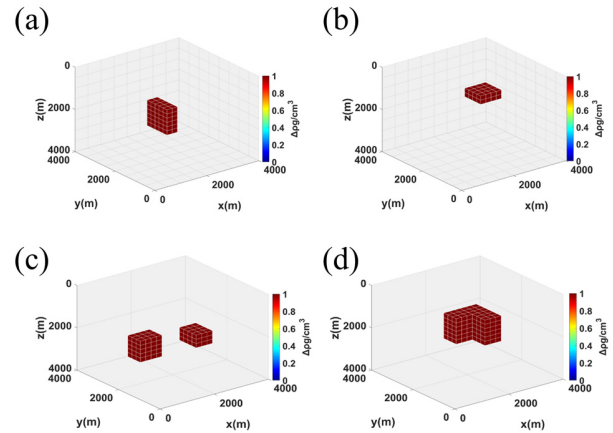

Fig. 2.   Visualization of 3-D density models for the purpose of training. (a) and (b) Example of a single model. (c) Example of two isolated models. (d) Example of a contact assembly model.

where (x, y, z) represents the corresponding coordinates of a ground observation point, (ξ, η, ζ) represents the spatial coordinates of a small square along x, y, and z direction, respectively, ρ represents the residual density of a small square, and $\partial V / \partial z$ is the derivative of the gravity potential on the z direction.

B. Structure of MS-UNet Network

In order to achieve the reconstruction of a 3-D density model based on gravity data, we have designed a neural network suitable for this purpose. Fig. 3 presents the overall network
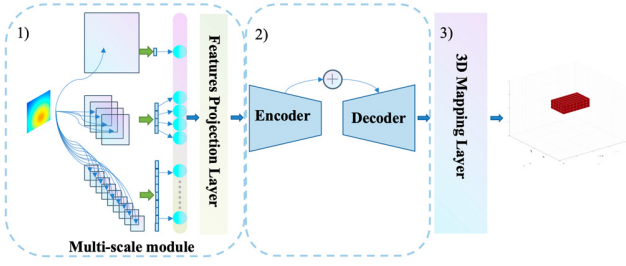
Fig. 3. Structure map of MS-UNet network. (1) (Left) Multiscale module whose function is implemented via a spatial pyramid pool. (2) (Middle) Fundamental structure of UNet network. (3) (Right) 3-D mapping layer whose function is to visualize inverted density data.
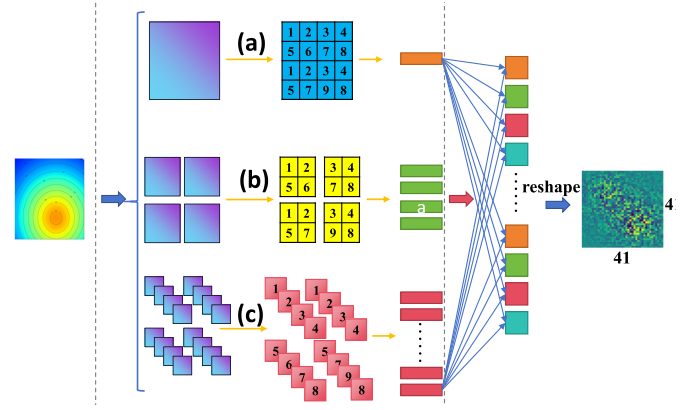

Fig. 4. Structure map of the multiscale module, dividing the input feature gravity field into three separate groups: (a) entire feature map, (b) four subfeature maps, and (c) 16 distinct feature maps. Each group is independently pooled to produce a $1 \times n$ eigenvector. Ultimately, these 21 feature vectors are combined to create an extensive 41×41 feature map.

architecture comprising a multiscale module, an encoder-decoder network, and a 3-D mapping layer.

1) Structure of Multiscale Module: In this study, the multi-scale feature shown in left part of the Fig. 3, is implemented via a spatial pyramid pool (see Fig. 4). This process segments the input feature map into three distinct categories: 1) one complete feature map, 2) four subfeature maps, and 3) 16 individual feature maps. Each segment undergoes independent pooling to yield a $1 \times n$ vector. The synthetic gravitational stations, which were separated by 100 m, were arranged along 21 survey lines with 100 m interline spacing, covering 4000×4000 m area. Finally, total 21 feature vectors are collectively mapped to form a comprehensive 41×41 feature map. The action of this module can be described as a standard operation of the neural network. The output of each neuron is given by the following equation:

$$\text{Output} = \delta \left(\sum_{k=0}^{C_{\text{in}}-1} \left(\text{weight}(k, C_{\text{out}}) \times \text{input}(N_i) \right) + \text{bias} \right) \quad (2)$$

where δ stands for the ReLU activation function, the input represents the input nodes from the previous layer, C_{in} represents the number of input nodes from the previous layer, the weight represents its corresponding connection weight, and the bias refers to an additional parameter in the neuron of a network that is used to adjust the output along with the weighted sum of the inputs to the neuron. The multiscale module enables the network to handle inputs of arbitrary size.

The primary objective of using pyramid pooling in this article is to obtain coarse-grained global information and fine-grained feature information during the training process, as well as to extract features from different perspectives and then aggregate them, which serves to enhance the robustness of the network [64], [65]. Gravity data usually contain large-scale trends important for understanding the overall structure and small-scale details critical for local accuracy. The multiscale module can extract the necessary features more efficiently by intelligently dividing the data into different scales. This means it can achieve the same or better results with less computational effort. This is crucial for large-scale data processing, model training, or deployment scenarios where resources are limited. The process of dividing data into different scales and efficiently extracting features is optimized to use fewer computational resources (e.g., CPU or GPU, RAM storage,

and network bandwidth) than a naive approach. In summary, for different gravity observation maps, the multiscale module (see Fig. 4) divides data of different scales and extracts features attributed to local and regional scales while reducing resource consumption.

The different scale data are merged after being mapped to the same size by an input encoder through a feature projection layer of a fully connected network. It does not mean that the gravity data are merged but that the features extracted at different scales have been fused. This stems from the inherent requirement of CNNs for a fixed dimensionality of the input dataset. The term *multiscale* is employed to denote the integration of features recovered at varying resolutions into cohesive structures. Subsequently, these synthesized structures propagate through successive neural network layers for further processing and refinement.

2) Structure of Encoder-Decoder Module: The encoder (see Fig. 5) comprises four groups of encoding blocks, each performing two operations, taking as its input the comprehensive feature vector output from the multiscale module. Each encoding block contains a convolutional layer, a batch normalization layer, and a Leaky ReLU activation function. After passing through two encoding blocks (marked as $\times 2$ in Fig. 5), the output is merged into a S-E block and downsampled while undergoing featured sampling through S-P module (detail in Section II-B4) and a connection operation. This network then processes the input to produce an output of 8000×1 density data.

3) Structure of S-E Module: The S-E module (see Fig. 6) is pivotal for intelligently recalibrating channel-wise features in processing gravity data. It accentuates crucial features by allocating higher weights to informative channels while concurrently mitigating noise and irrelevant elements by attenuating their corresponding channels. This selective emphasis and suppression streamline the network's operations, enhancing its ability to discern intricate patterns in gravity data, which are essential for geophysical analysis. The S-E operation compresses the input $U \in \mathbb{R}^{H \times W \times C}$ into a vector $F_{\text{sq}}(u_c)$
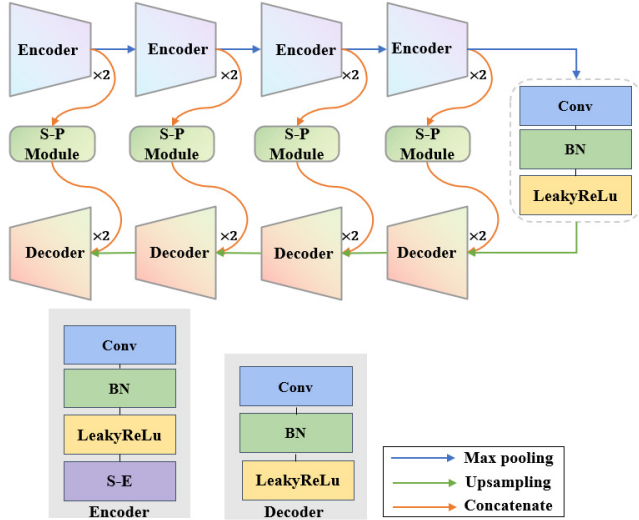
Fig. 5. Encoder-decoder network consisting of four encoding and decoding block groups. Each group processes the extensive feature vector output from the multiscale module through two primary operations. Within each block, the sequence includes a convolutional layer, batch normalization, and leaky ReLU activation.
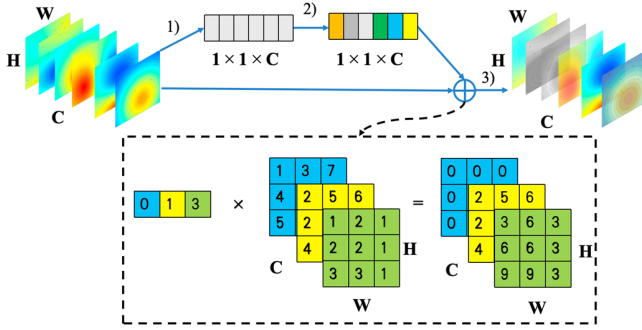

Fig. 6. Structure map of S-E module. Module operation: (1) feature map $(H \times W \times C)$ transforms to $1 \times 1 \times C$ vector via squeeze's global pooling. (2) Linear layer of excitation phase assesses channel importance. (3) Channel weights, calculated in the scale phase, are multiplied with their respective 2-D matrices in the original feature map.

through global pooling, as shown in the following equation:

$$F_{\text{sq}}(u_c) = \frac{1}{H \times W} \sum_{i=1}^{H} \sum_{j=1}^{W} u_c(i, j) \tag{3}$$

where $u_c(i, j)$ represents the cth element in the input $U \in \mathbb{R}^{H \times W \times C}$. H and W represent the numbers of the row and column of the extracted gravity input data by convolution operation throughout the designed number of channels (C), respectively. The operations within the module are detailed as follows: initially, the feature map of dimensions $H \times W \times C$ undergoes transformation into a $1 \times 1 \times C$ vector through global pooling in the squeeze phase. Subsequently, the excitation phase involves a linear layer predicting the significance of each channel. The final step involves multiplying the weights of each channel, determined in the scale part, with the 2-D matrix corresponding to each channel in the original feature map. Essentially, the SE module functions as an attention mechanism, adeptly learning the weights of each channel. This feature proves particularly effective in processing gravity data.

In order to capture channel-level dependencies, which refer to the assignment of larger weights to key feature maps within a feature channel to stimulate important features and suppress unimportant ones during feature extraction, the excitation operation generates a weight value for each feature channel. It implements two fully connected layers. The output is obtained by multiplying each channel with its corresponding channel weight. The mapping output formula is represented in the following equation:

$$s = F_{\text{ex}}(z, W) = \sigma(W_2 \delta(W_1 z)) \tag{4}$$

where z represents a single 2-D tensor as an element of $X \in \mathbb{R}^{H \times W}$ of the input $U \in \mathbb{R}^{H \times W \times C}$ and σ represents the sigmoid function. The weight matrices are denoted as $W_1 \in \mathbb{R}^{(C/r) \times c}$ and $W_2 \in \mathbb{R}^{(C/r) \times c}$, where the hyperparameter r determines the compression ratio of parameters in the first fully connected layer. The S-E block accurately learns channel correlations to enhance sensitivity to important channels and suppress redundant or irrelevant features, which may even act as noise, potentially hampering the performance of the prediction [66], [67], [68].

Removing the S-E module from the MS-UNet network will likely diminish its ability to emphasize important features and suppress less relevant ones, potentially leading to decreased accuracy and generalization capability. While this simplifies the network's architecture, it may also make the network more sensitive to variations and noise in the input data, affecting its overall performance.

4) Structure of S-P Module: Traditional pooling operations in CNNs, such as max pooling and average pooling, have been widely used to reduce the spatial dimension of feature maps, thereby allowing the model to learn higher-level abstract features. However, these operations often lead to a loss of spatial resolution and fine-grained details, which can be particularly problematic when attempting to capture thin, strip-like structures often encountered in geophysical data (e.g., thin geological layers, faults, and fractures).

The S-P module (see Fig. 7) is designed to overcome this limitation by maintaining high-resolution information. It introduces an extra pooling branch that maintains the same resolution as the original input, allowing the model to capture global and local information [69]. By leveraging the S-P module, the network is able to better retain and learn from the fine-grained, strip-like structures in the data, thereby potentially improving the accuracy of geophysical inversion. It takes the average of a row or column of values in the 2-D tensor using $(H, 1)$ and $(1, W)$ S-P operations, respectively. This is because traditional pooling techniques only focus on the correlation between convolutional kernel senses and are not sensitive to long-distance correlations. Consequently, employing S-P operations emerges as a viable strategy to adeptly extract features characterized by heterogeneous orientations, scales, and separations, thus capturing the multidimensional intricacies of the data. Therefore, the output of the S-P module, $y^h \in \mathbb{R}^H$ and $y^w \in \mathbb{R}^W$, can be represented by the following
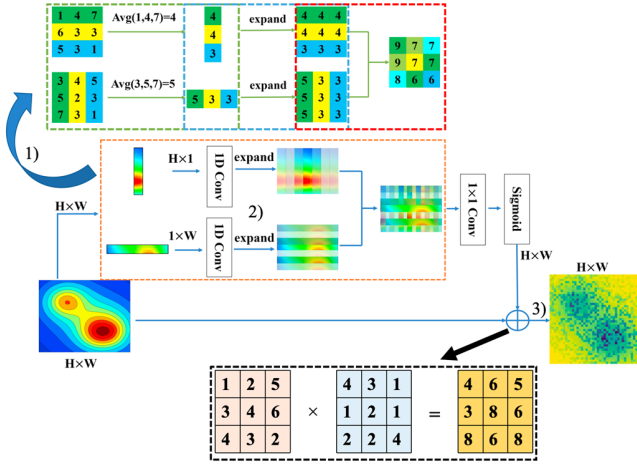
Fig. 7. Structure map of S-P module. (1) Horizontal average pooling: take out each row of data in the feature map ($n \times n$) for average operation (e.g., Avg(1, 4, 7) = (1 + 4 + 7)/3 = 4). Vertical average pooling: take out each column of data in the feature map for average operation (e.g., Avg(3, 5, 7) = (3 + 5 + 7)/3 = 5). (2) By averaging pooling horizontally and vertically, $n \times 1$ and $1 \times n$ feature vectors are obtained. The feature vectors are expanded to the original size of the feature map through expansion, where $n \times 1$ copies n columns to $n \times n$ and $1 \times n$ copies n rows to $n \times n$. (3) Add the corresponding positions of the two $n \times n$ feature maps that have been expanded.

equations:

$$y_i^h = \frac{1}{W} \sum_{0 \le j < W} x_{i,j} \tag{5}$$

$$y_j^w = \frac{1}{H} \sum_{0 \le i < H} x_{i,j} \tag{6}$$

where $j \in [H, 1]$ and $i \in [1, W]$ are the row and column indices, respectively.

The process unfolds in the following manner: initially, the S-P module averages across the horizontal and vertical dimensions of space. Next, the resulting $H \times 1$ and $1 \times W$ vectors are expanded and then concatenated to form a single vector. The final step involves multiplying the obtained $H \times W$ feature map with the original feature map, postconvolution, and sigmoid operation. Unlike maximum and average pooling, the S-P module focuses on a longer, narrower range, enabling the network to efficiently simulate long-distance dependencies.

Subsequently, the decoder is composed of four groups of decoding blocks. During decoding, in contrast to traditional concatenation methods, we utilize a two-stage concatenation scheme, first concatenating with the feature map extracted by the S-P module and then concatenating with the upsampled feature map. Then, after convolution, normalization and ReLU activation functions are applied. The output image from the decoder passes through a fully connected feedforward 3-D mapping layer. This mapping process might involve various assumptions about the underlying geology and the relationship between gravity measurements and density variations. The neural network is essentially learning these relationships during training through the use of supervised learning labels, which represent the density distribution in the inversion domain. Finally, the network applies its learned knowledge to form the predicted density model.
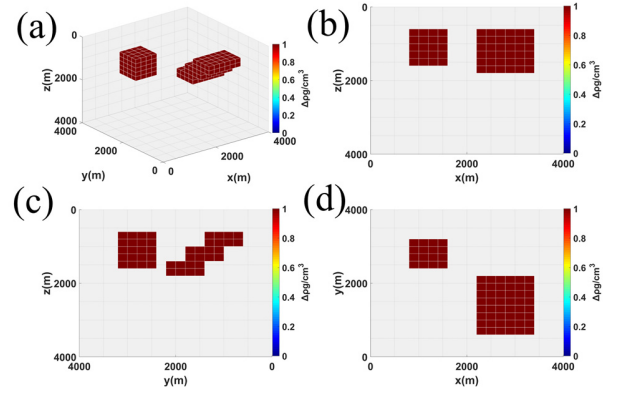

Fig. 8. Example of contact density model for the purpose of training. (a) 3-D view model, (b) X–Z view model, (c) Y–Z view model, and (d) X–Y view model.

5) Termination of the Training: To verify the stability of various UNet-based networks, this article employs normalized misfit to illustrate the gravity observation loss during the training. The specific formula for the normalized misfit is as follows:

$$\text{misfit} = \frac{\left\| g^{\text{True}} - g^{\text{Pred}} \right\|^2}{\left\| g^{\text{True}} \right\|^2} \tag{7}$$

where $\|\cdots\|$ stand for norm operator, g^{True} denotes the theoretical observed gravity data, g^{Pred} represents the predicted gravity data, and misfit stands for the normalized error of gravity anomalies. During the process of the training, it tabulates the accuracy of gravity anomalies at all observation points.

III. SYNTHETIC MODEL STUDIES

A. Synthetic Model Study

To assess the recognition accuracy of the network, we designed relatively simple simulation models. Fig. 8 shows the location and details of a randomly selected contact assembly model, which consists of a rectangle and a trapezoid. The upper and lower bodies have a density of 1.0 g/cm^3. The observation area extends from 0 to 4000 m in the x-direction and from 0 to 4000 m in the y-direction, with a 100-m interval between data points, resulting in 1681 data points for each component of the gravity gradiometry tensor. The 3-D volume of the inversion domain was divided into 8000 cubic cells ($20 \times 20 \times 20$) with a side length of 200 m. For clarity, all 3-D views in the subsequent experiments display only parts with a density value greater than 0.5 g/cm^3.

To ensure consistent results across various network configurations, we standardized the hyperparameters for each network variant. Table I outlines these hyperparameters, which encompass the learning rate (LR), LR schedule, batch size, epoch count, optimizer type, and the GPU model used for training. For example, all network variations, including UNet, UNet + S-E, UNet + S-P, and MS-UNet, were uniformly trained with a LR of 0.001, employing cosine annealing for LR adjustment, a batch size of 24, across 100 epochs, using the Adam optimizer on an RTX3080 GPU. This detailed description of our training approach offers a comprehensive view of the operational settings for each network, enhancing

TABLE I
HYPERPARAMETER SETTINGS BASED ON FOUR NETWORKS

Network Parameters	Settings
Learning rate	0.001
LR schedule	Cosine Annealing
Batch size	24
Epoch	100
Optimizer	Adam
GPU type	RTX3080

the clarity and comparability of our training and evaluation process.

Fig. 9(a) presents 3-D views of the model. Fig. 9(b) shows the results recovered by the UNet network. One can see that the predicted model is consistent with the actual model. However, the cubic body prediction could be better. There are also slight differences in residual density at the edge of the high-level step of the trapezoid, and there are also differences between the top and bottom of the cube. By adding the S-E module [see Fig. 9(c)], the overall shape information becomes more consistent with the actual model. Compared to UNet networks, the outline boundaries are more clear, especially the prediction of residual density at the top of the cube, which is more in line with the actual model. In Fig. 9(d), the predicted density information for U-Net networks with S-P module is more accurate, and the density is closer to the theoretical value from the X–Y and Y–Z views. From the x–z view, it can be seen that the missing edge cells that UNet cannot predict are shown to some extent. However, there is a similar problem with the redundant density units at the bottom, as in the cube model of UNet prediction. The MS-UNet network performs the best in inversion modeling [see Fig. 9(e)], with the density value almost identical to the actual model, resulting in excellent inversion results.

Fig. 10 shows the corresponding normalized misfit behavior of the predicted gravity anomaly against the actual gravity data by (7). For traditional UNet, the normalized misfit of gravity anomalies is above 20% [see Fig. 10(a)]. This significant discrepancy is largely attributed to the erroneous inversion of an anomalous body that does not actually exist. Additionally, this anomaly is not intersected by the vertical section at $Y = 1800$ m, as depicted in Fig. 9. After adding the S-E module, the normalized misfit of residual density units is significantly improved [see Fig. 10(b)], indicating that adding the S-E module in downsampling preserves more important original information. The fitting increased after adding the S-P module [see Fig. 10(c)] indicating that the two concatenation operations allowed for more fusion of high and low features. The MS-UNet network demonstrates a highly accurate fit with minimal error. However, there was still room for improvement in improving misfit, indicating that there was still some information loss during downsampling.

B. Multiscale Study

To simulate real-world conditions in our study, we introduced independent 5% Gaussian noise into the synthetic
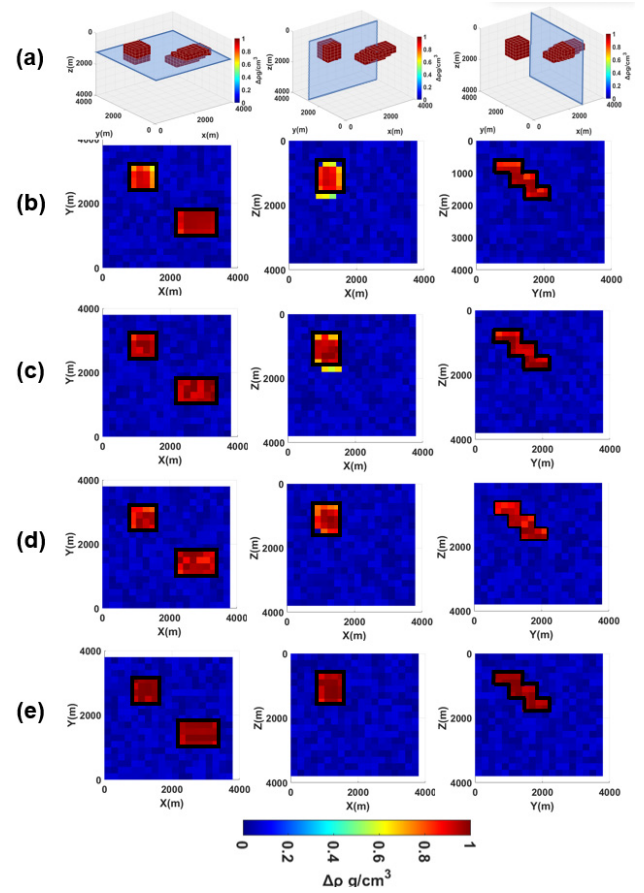

Fig. 9. Comparison of prediction results of different networks under different sections [(First column) Horizontal section at $Z = 1800$ m. (Second column) Vertical section at $Y = 1800$ m. (Third column) Vertical section at $X = 2800$ m]. (a) 3-D views of the model, (b) model recovered by UNet network, (c) model recovered by UNet + S-E network, (d) model recovered by UNet + S-P network, and (e) model recovered by MS-UNet network.
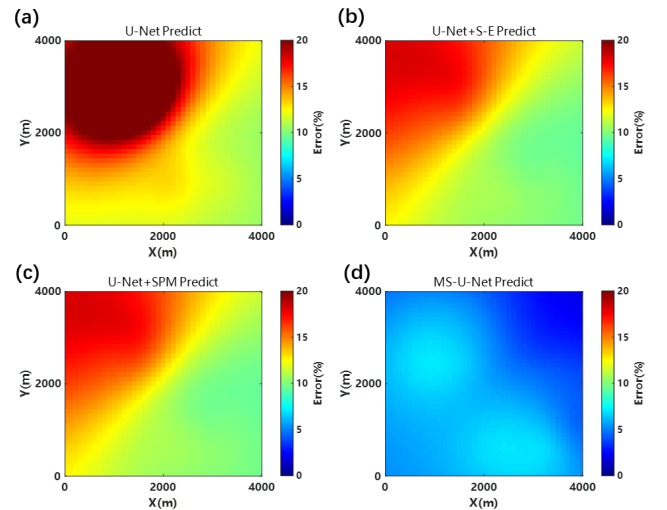

Fig. 10. Comparison normalized misfit of gravity field forwarded by density model predicted by four different network models using (a) UNet network, (b) UNet + S-E network, (c) UNet + S-P network, and (d) MS-UNet network.

observed data, as shown in Fig. 11. This modified data was then processed using the MS-UNet network to invert the synthetic density model. Our analysis, highlighted in Fig. 12(a) and (b), reveals a striking similarity in the residual
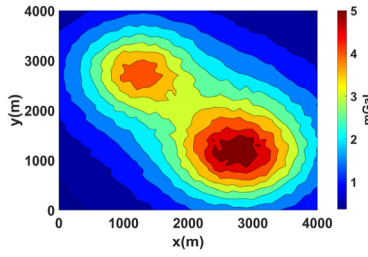
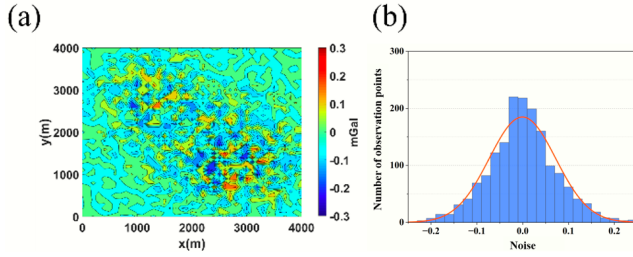Fig. 11. Gravity anomaly map with 5% independent Gaussian noise.

Fig. 12. Noise robustness analysis using the MS-UNet network based on independent Gaussian noise, accounting for 5% of observed data contamination. (a) Random distribution of the noise and its amplitude. (b) Number of observations and the size of the noise conform to the normal distribution.

distribution between the gravity data predicted by the MS-UNet network and the original noisy data, demonstrating the network's robustness to noise.

In conventional UNet architectures, the precise alignment of data dimensions during the concatenation process is crucial. It is often necessary for the test data to have the same dimension size as the training set to ensure the network's proper functioning and accuracy. During the downsampling process, convolution and pooling operations are employed. If the input field graph is not evenly divisible, these operations will round down, leading to some feature loss during both the downsampling and upsampling stages. Consequently, a reshape operation is typically implemented before the multiscale field graph is inputted into the UNet model. This ensures compatibility with the network's requirements and mitigates potential feature loss. However, in practice, obtaining a complete gravitational field that fulfills the aforementioned conditions can often prove challenging, since the observed gravity data are often unevenly distributed, with some areas having no data.

The traditional UNet model processes data from the entire space directly, and any missing data can significantly impact the network's accuracy. To address this issue, we designed the multiscale module. We tested the inversion ability of this module on simulated geology with some areas blocked by the river (e.g., channel obstruction) and on a complex observation map with randomly missing data points to evaluate its performance. Fig. 13 shows the gravity anomaly map for the two different scenarios marked by white areas.

Fig. 14 displays the multiscale inversion results obtained for various geological conditions simulated in this study involving the two different scenarios shown in Fig. 13. Notably, the network achieves a certain degree of accuracy in inverting data for different scenarios and successfully identifies the position and density of anomalous bodies that generally match
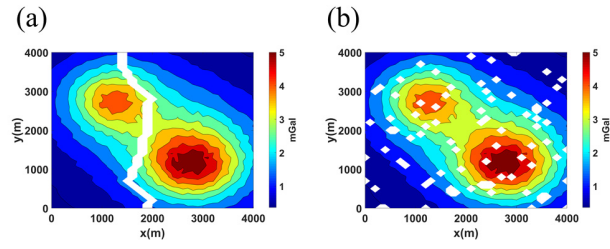

Fig. 13. Gravity data with independent 5% Gaussian noise in two different acquisition scenarios. (a) Gravity anomaly data based on channel obstruction. (b) Gravity anomaly data based on random missing observation points.
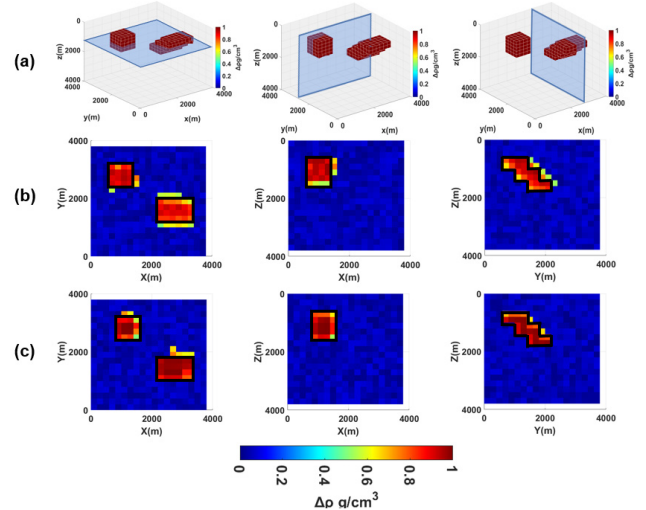

Fig. 14. Comparison of inversion results recovered by MS-UNet network along different cutting sections by (first column) $Z = 1800$ m, (second column) $Y = 3000$ m, and (third column) $X = 1800$ m with (a) 3-D true model view, (b) simulated channel obstruction, and (c) random missing observation points.

the true models. Therefore, in the case involving randomly missing measurement points, the predicted residual density of the gravity anomaly volume model and its corresponding theoretical unit exhibits excellent robustness and precision of around 90%.

However, numerous excess density units appear at the model's edge. The density distribution is relatively accurate, with deviation units concentrated outside the edge contour. Additionally, the fuzzy units at the edge have a density of about 0.5 g/cm^3, similar to the background density (below 0.5 g/cm^3), resulting in a relatively low impact on accuracy. The simulation results of river blockage suggest that, despite the disrupted data, the MS-UNet network can accurately predict the cube's position. From the perspective of spatial distribution, the inversion model aligns with the theoretical model results. However, a more in-depth examination reveals an apparent blurring of the edge contour, with significant differences in the results of residual density inversion at the edge.

Fig. 15 depicts the comparison of the normalized misfit of the inversion results obtained under the two different acquisition scenarios with various data dimensions. Despite the random missing points, the average normalized misfit of the gravity anomaly stands around 10% [see Fig. 15(b)]. In contrast, the average normalized misfit for the river obstruction
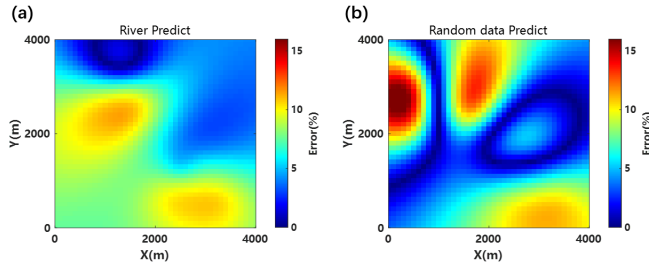
Fig. 15. Comparison normalized misfit of gravity field forwarded by density model predicted under the two different acquisition scenarios, as (a) simulated river obstruction and (b) random missing observation points.
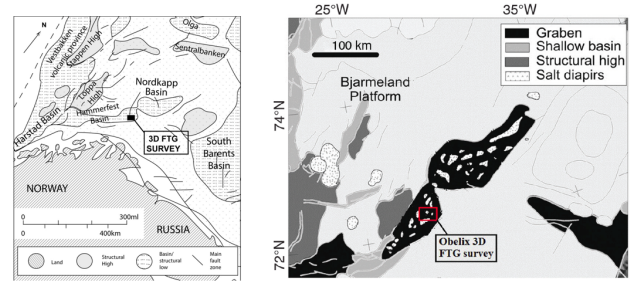

Fig. 16. (a) Main structural elements in the Barents Sea area, location of Nordkapp Basin, and 3-D FTG survey. Modified from Johansen et al. [76]. (b) Simplified structural map of the Nordkapp basin showing salt diapirs and main fault zones. Black zones show subcrops of diapirs at or near the Pliocene-Pleistocene unconformity. Modified from Zhdanov and Lin [77].

decreases around 5% [see Fig. 15(a)]. These results effectively demonstrate that employing the MS-UNet network enhances the model's robustness and imparts a degree of tolerance for missing data. In comparison with the traditional UNet model, our proposed network demonstrates superior accuracy when confronted with partial data loss. This advancement is notably significant in addressing the issue of missing data in real-world datasets.

IV. CASE STUDY

A. Geological Characteristics of the Area of a 3-D Marine FTG Survey

The Nordkapp Basin, located in the Barents Sea, has a complex geological history shaped by multiple tectonic, sedimentary, and volcanic activities. Its stratigraphic record spans from the late Paleozoic to the Cenozoic era, marking significant geological events such as the formation of the supercontinent Pangea and its subsequent breakup. The stratigraphy of the Nordkapp Basin is characterized by a series of sedimentary layers, each representing different geological periods. The lowermost layers are primarily composed of late Paleozoic sediments, rich in carbonate and clastic deposits [70], [71]. Above these are Mesozoic sediments, which include a mix of shale, sandstone, and carbonate formations [72], [73]. The upper layers consist of Cenozoic deposits, mainly dominated by glacial and postglacial sediments [74].

The F2 salt diapirs within the Nordkapp Basin are primarily a result of the movement and deformation of Zechstein salt layers, which date back to the late Permian period. These salt layers, initially deposited in a relatively flat and uniform manner, were later subjected to tectonic forces that led to their mobilization and eventual formation of diapiric structures. The tectonic evolution of the Nordkapp Basin, including episodes of extension and compression, played a crucial role in the formation of these salt structures. Salt migration and diapirism were influenced by differential loading due to sedimentation, variations in subsurface temperatures, and tectonic stress regimes [75].

The full-tensor gradient (FTG) survey was conducted in the Nordkapp Basin, offshore Norway, in the Barents Sea [see Fig. 16(a)]. The Nordkapp Basin can be partitioned into the southwestern part (SWP) and the northeastern part (NEP). The SWP subbasin, located at the Obelix survey site, is a narrow geological structure that is 150 km long and 25–50 km wide, with a trend toward the northeast. It is characterized by

over 17 complex salt diapirs, representing the predominant geological structures of the area [as shown in Fig. 16(b)]. On the other hand, the NEP subbasin spans approximately 200 km in length and 50–70 km in width and contains more than 16 salt structures. Hydrocarbon exploration activities in the Nordkapp basin were initiated in the 1980s. So far, three wells have been drilled, all located on the flanks of the basin. Recent geological and geophysical surveys and the discovery of hydrocarbon deposits in wells outside the basin suggest that the potential for identifying hydrocarbon reservoirs within the Nordkapp basin exists.

The primary geological objectives are the F2 salt diapirs, identifiable by the lack of well-defined seismic horizons (see Fig. 17). With advancements in seismic methodology and structural interpretation, the mapping of salt structures in the Nordkapp Basin has become increasingly complex, with salt stocks exhibiting vertical flanks replaced by shapes with broad diapir overhangs atop narrow stems. Nonetheless, seismic depth migration images are usually distorted (as shown in Fig. 18) due to salt features and the underdetermined inversion models of the salt isopach (which ultimately limits the capability to obtain a mapping of the salt base through seismic tools). In this regard, the FTG survey offered supplementary information for evaluating these intricate salt overhang structures. The FTG technique is an ideal approach to such problems as it is susceptible to geological anomalies featuring significant density contrasts. Statoil provides two types of salt base interpretations: one that is derived from seismic data, marked by a solid purple line, and another that is derived from FTG data, marked by a red dashed line [78]. These two salt base interpretations will be employed to recognize and validate the inversion results.

Overcoming this challenge necessitates the application of a meticulous 3-D inversion of the FTG data. Various publications have focused on the sharp boundary inversion of the FTG data in the Nordkapp Basin utilizing focusing regularization [22], [23], [77], [78]. This article only uses the vertical component of gravity field g_z, instead of FTG data to presents the initial findings of inversion utilizing MS-UNet, which can establish a connection between labels, geological models, trained data, and predicted data to resolve sharp density contrasts between salt structures and the adjacent host rock.
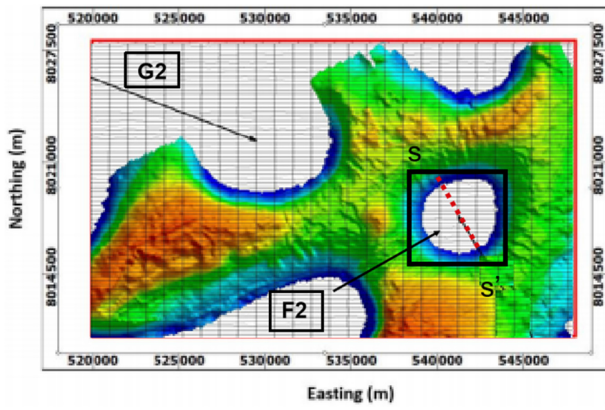
Fig. 17. Obelix 3-D FTG Survey Grid with Seismic Horizons. The main geological targets are the salt diapirs G2 and F2, which are manifested by the absence of well-resolved seismic horizons. The area remarked by the solid red line is the original FTG survey grid. The subset marked by a solid black line of the original FTG data focuses on the F2 salt diapir areas. The seismic line is represented S-S′ by the red dashed line.
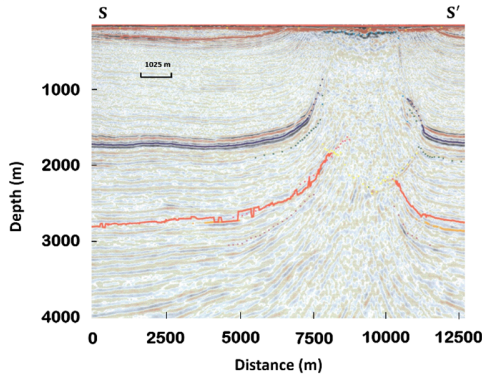

Fig. 18. Seismic Trace (S-S′) depth migrated profile from 3-D survey showing salt feature F2 and typical imaging ambiguity of high resolution seismic. Modified from Xu et al. [78].

B. Results

Given that the primary geological target is the F2 salt diapir, we selected a subset (i.e., the vertical component of gravity field) from the initial FTG dataset to concentrate on the salt dome areas highlighted by the F2 marker. This article presents the inversion findings as a vertical cross-sectional overlay comparison of the S-S seismic profile.

In this initial practical application of the MS-UNets Network, we conducted the inversion using the vertical component of the gravity field g_z for simplicity as input data. For the inversion domain, we opted for a 4 km (east-west, x-axis) × 4 km (north-south, y-axis) area that continued to a depth of 4 km (z-axis). The inversion volume consisted of 8000 discretization cells with a size of 20 × 20 × 20 m. The training lasted approximately 30 min, while the prediction time was roughly 4 s.

Fig. 19(a) shows the area of the observed data used for inversion. The multiscale module imposes no restrictions on the size of the observation surface or the number of observation points. Fig. 19(b) presents the predicted observed gravity data map reconstructed using the MS-UNet network, which resembles the actual observed data.

To assess the accuracy of the results, we projected the inversion density onto the corresponding S-S profile of the
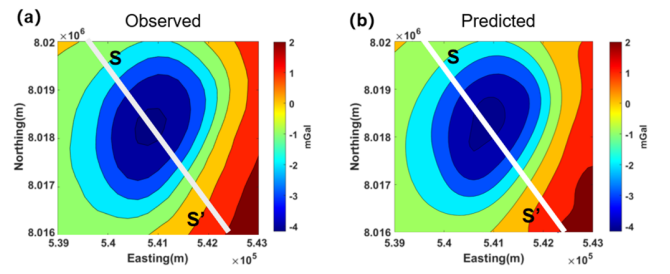

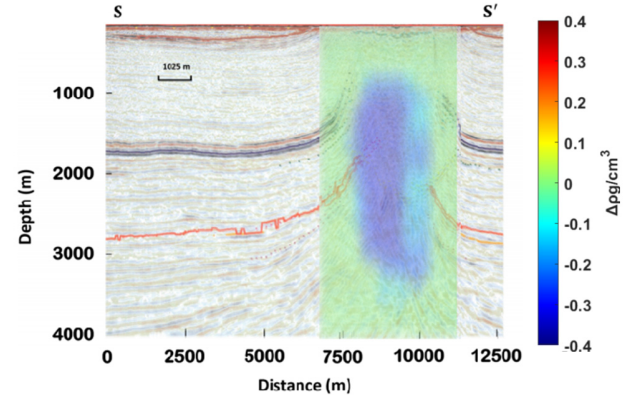Fig. 19. Comparison of (a) observed gravity data and (b) predicted gravity data.

Fig. 20. Density profile generated by the MS-UNet reconstruction model along the seismic line profile.

seismic trace and conducted overlay comparison (see Fig. 20). One can see that the MS-UNet network reconstruction model agrees with the seismic interpretation data well. The model produced by the MS-UNet inversion describes a distinct salt dome geometry.

V. CONCLUSION

The MS-UNet network has strong potential for practical application in geophysical data analysis, structural reconstruction, and inversion, using its DL abilities. It operates without applying the mathematical equations or physical laws that describe the relationship between the models and observed data. This article proposes the MS-UNet network, which quickly establishes the relationship between labels, geological models, trained data, and predicted data, resulting in improved accuracy and speed of subsurface physical property imaging.

To validate the proposed MS-UNet inversion network, we employed a composite model with uniform density contrast. The trained MS-UNet networks can effectively restore the detailed structure of isolated density anomalies and reconstruct the true density values of the models. Furthermore, we demonstrated the robustness of the MS-UNet network to multiscale data.

In practical applications, the MS-UNet network successfully predicted the geometry and density of salt diapir in the Nordkapp basin. Additionally, the model reconstructed from the trained MS-UNet network showed that the boundaries of salt diapir (F2) with relatively sharp density contrast closely resembled the interpreted salt boundaries from seismic data. These results demonstrate the potential of the MS-UNet

network in geophysical data analysis, structural reconstruction, and inversion.

REFERENCES

[1] A. S. Abu-El Ata, A. E. Ghonimi, and A. H. Hafeez, "Geologic causatives and seismic attributes heterogeneities for structural and stratigraphic interplays," Sitra Area, North Western Desert, Egypt, pp. 41–51, 2023, vol. 41, no. 6.

[2] A. Chugaev et al., "The integrated borehole seismic surveys at the verkhnekamskoye potassium salt deposit," in *Proc. Int. Perm Forum Sci. Global Challenges 21st Century*, 2022, pp. 255–269.

[3] J. C. D. S. Vital, M. V. B. Ade, R. Morelatto, and W. M. Lupinacci, "Compartmentalization and stratigraphic-structural trapping in pre-salt carbonate reservoirs of the Santos Basin: A case study in the Iara complex," *Mar. Petroleum Geol.*, vol. 151, May 2023, Art. no. 106163.

[4] J. Casacão, F. Silva, J. Rocha, J. Almeida, and M. Santos, "Aspects of salt diapirism and structural evolution of Mesozoic–Cenozoic basins at the West Iberian margin," *AAPG Bull.*, vol. 107, no. 1, pp. 49–85, Jan. 2023.

[5] G. Chen, W. Yang, Y. Liu, H. Wang, and X. Huang, "Salt structure elastic full waveform inversion based on the multiscale signed envelope," *IEEE Trans. Geosci. Remote Sens.*, vol. 60, 2022, Art. no. 4508912.

[6] M. Kalita, V. Kazei, Y. Choi, and T. Alkhalifah, "Regularized full-waveform inversion with automated salt flooding," *Geophysics*, vol. 84, no. 4, pp. 569–582, Jul. 2019.

[7] P. Zhang, R.-S. Wu, L. Han, and Y. Zhou, "Strong-scattering multiparameter reconstruction based on elastic direct envelope inversion and full-waveform inversion with anisotropic total variation constraint," *Remote Sens.*, vol. 15, no. 3, p. 746, Jan. 2023.

[8] Y. Bao, Y. Wang, G. Deng, and Q. Mao, "Elastic wave pre-stack reverse-time migration based on the second-order P- and S-wave decoupling equation," *J. Geophys. Eng.*, vol. 19, no. 5, pp. 1221–1234, Oct. 2022.

[9] P. Kuzmenko et al., "Some aspects of seismic data reverse time migration for salt tectonics geology of the dnieper-donets basin," *Proc. SPIE*, Nov. 2021, Art. no. SPE-208531-MS.

[10] S. Coskun, R. R. Stewart, E. Baysal, and A. Aydemir, "Optimum designs for 2-D and 3-D seismic surveys via modeling and reverse-time migration: Pierce junction salt dome, Texas," *Surv. Geophys.*, vol. 42, no. 5, pp. 1171–1196, Sep. 2021.

[11] S. Ziramov, C. Young, J. Kinkela, G. Turner, and M. Urosevic, "Pre-stack depth imaging techniques for the delineation of the Carosue Dam gold deposit, Western Australia," *Geophys. Prospecting*, pp. 1071–1384, Jan. 2023.

[12] J. Herwanger, A. Bottrill, and M. Oristaglio, "Salt geomechanics and seismic velocity models," in *Proc. 1st EAGE Workshop Pre-Salt Reservoir, Explor. Production*, 2019, pp. 1–5.

[13] N. Yang, G. Li, P. Zhao, J. Zhang, and D. Zhao, "Porosity prediction from pre-stack seismic data via a data-driven approach," *J. Appl. Geophys.*, vol. 211, Apr. 2023, Art. no. 104947.

[14] M. M. Gonçalves and E. P. Leite, "Cooperative inversion of seismic reflection and gravity data: An object-based approach," *J. Appl. Geophys.*, vol. 167, pp. 42–50, Aug. 2019.

[15] J. Hao, S. Wu, J. Yang, Y. Zhang, and X. Sha, "Application of seismic waveform indicator inversion in the depth domain: A case study of pre-salt thin carbonate reservoir prediction," *Energies*, vol. 16, no. 7, p. 3073, Mar. 2023.

[16] C. H. Henke, M. H. Krieger, K. Strack, and A. Zerilli, "Subsalt imaging in northern Germany using multiphysics (magnetotellurics, gravity, and seismic)," *Interpretation*, vol. 8, no. 4, pp. 15–24, Nov. 2020.

[17] D. Abdelfattah, "New semi-inversion method of Bouguer gravity anomalies separation," in *Gravitational Field-Concepts and Applications*. London, U.K., 2022, p. 113.

[18] H. Ghari, R. Varfinezhad, and S. Parnow, "3D joint interpretation of potential field, geology, and well data to evaluate a salt dome in the Qarah-Aghaje Area, Zanjan, NW Iran," *Near Surf. Geophys.*, vol. 21, no. 3, pp. 233–246, Jun. 2023.

[19] L. Gernigon, M. Brönner, C. Fichler, L. Løvas, L. Marello, and O. Olesen, "Magnetic expression of salt diapir-related structures in the Nordkapp Basin, Western Barents Sea," *Geology*, vol. 39, no. 2, pp. 135–138, Feb. 2011.

[20] C. Stadtler, C. Fichler, K. Hokstad, E. A. Myrlund, S. Wienecke, and B. Fotland, "Improved salt imaging in a basin context by high resolution potential field data: Nordkapp Basin, Barents Sea," *Geophys. Prospecting*, vol. 62, no. 3, pp. 615–630, May 2014.

[21] V. Paoletti, M. Milano, J. Baniamerian, and M. Fedi, "Magnetic field imaging of salt structures at Nordkapp Basin, Barents Sea," *Geophys. Res. Lett.*, vol. 47, no. 18, Sep. 2020, Art. no. e2020GL08902.

[22] M. Tao, M. Jorgensen, and M. S. Zhdanov, "Mapping the salt structures from magnetic and gravity gradiometry data in Nordkapp Basin, Barents Sea," in *Proc. 1st Int. Meeting Appl. Geosci. Energy*, 2021, pp. 874–878.

[23] X. Tu and M. S. Zhdanov, "Joint focusing inversion of marine controlled-source electromagnetic and full tensor gravity gradiometry data," *Geophysics*, vol. 87, no. 5, pp. 35–47, Sep. 2022.

[24] M. S. Zhdanov, X. Tu, and M. Cuma, "Cooperative inversion of multiphysics data using joint minimum entropy constraints," *Near Surf. Geophys.*, vol. 20, no. 6, pp. 623–636, Dec. 2022.

[25] M. Jorgensen, M. Zhdanov, and B. Parsons, "3D focusing inversion of full tensor magnetic gradiometry data with Gramian regularization," *Minerals*, vol. 13, no. 7, p. 851, Jun. 2023.

[26] Z. Xu et al., "Inversion of the gravity gradiometry data by ResUet network: An application in Nordkapp Basin, Barents Sea," *IEEE Trans. Geosci. Remote Sens.*, vol. 61, 2023, Art. no. 4502410.

[27] X. Wei and J. Sun, "Uncertainty analysis of 3D potential-field deterministic inversion using mixed lp norms," *Geophysics*, vol. 86, no. 6, pp. 133–158, Nov. 2021.

[28] X. Wei, J. Sun, and M. K. Sen, "Quantifying uncertainty of salt body shapes recovered from gravity data using trans-dimensional Markov chain Monte Carlo sampling," *Geophys. J. Int.*, vol. 232, no. 3, pp. 1957–1978, Nov. 2022.

[29] A. Melo and Y. Li, "Geology differentiation by applying unsupervised machine learning to multiple independent geophysical inversions," *Geophys. J. Int.*, vol. 227, no. 3, pp. 2058–2078, Jul. 2021.

[30] V. V. Vesselinov, M. K. Mudunuru, B. Ahmmed, S. Karra, and R. S. Middleton, "Discovering signatures of hidden geothermal resources based on unsupervised learning," in *Proc. 45th Workshop Geothermal Reservoir Eng.* Stanford, CA, USA: Stanford University, Feb. 2020, Paper SGP-TR-216.

[31] Z. Xu, G. Zou, Q. Wei, J. Tian, and H. Yuan, "Focusing joint inversion of gravity and magnetic data using a clustering stabilizer in a space of weighted parameters," *Geophys. J. Int.*, vol. 224, no. 2, pp. 1344–1359, Nov. 2020.

[32] E. Amirian, J. Y. Leung, S. Zanon, and P. Dzurman, "Integrated cluster analysis and artificial neural network modeling for steam-assisted gravity drainage performance prediction in heterogeneous reservoirs," *Exp. Syst. Appl.*, vol. 42, no. 2, pp. 723–740, Feb. 2015.

[33] S. M. Iveson, M. Mason, and K. P. Galvin, "Gravity separation and desliming of fine coal: Pilot-plant study using reflux classifiers in series," *Int. J. Coal Preparation Utilization*, vol. 34, no. 5, pp. 239–259, Sep. 2014.

[34] S. Chander and D. Ganguly, "Development of water level estimation algorithms using SARAL/Altika dataset and validation over the Ukai Reservoir, India," *J. Appl. Remote Sens.*, vol. 11, no. 1, Jan. 2017, Art. no. 016012.

[35] N. Tavakolizadeh and M. Bagheri, "Multi-attribute selection for salt dome detection based on SVM and MLP machine learning techniques," *Natural Resour. Res.*, vol. 31, no. 1, pp. 353–370, Feb. 2022.

[36] F. Abedi et al., "Salt dome related soil salinity in southern Iran: Prediction and mapping with averaging machine learning models," *Land Degradation Develop.*, vol. 32, no. 3, pp. 1540–1554, Feb. 2021.

[37] D. Lubo-Robles, T. Ha, J. Qi, Y. Kim, and K. J. Marfurt, "Machine learning applications using seismic attributes—A hands-on course—Part 5D: Attribute selection using Gaussian mixture models and random forest decision trees,"

[38] G. Alhabib, G. Latif, J. Alghazo, and G. B. Brahim, "Seismic structures classification using novel features from seismic images," in *Proc. 14th Int. Conf. Comput. Intell. Commun. Netw.*, 2022, pp. 96–102.

[39] S. R. Ford and D. S. Dreger, "Pre-sinkhole seismicity at the napoleonville salt dome: Implications for local seismic monitoring of underground caverns," *Seismological Res. Lett.*, vol. 91, no. 3, pp. 1672–1678, May 2020.

[40] G. Florio, M. Fedi, and F. Cella, "A fractional vertical derivative technique for regional-residual separation," *Geophys. J. Int.*, vol. 232, no. 1, pp. 601–614, Oct. 2022.

[41] R. Baardman and C. Tsingas, "Classification and suppression of blending noise using convolutional neural networks," *Proc. SPIE*, Mar. 2019, Art. no. SPE-194731-MS.

[42] Z. H. Zhang et al., "Deep learning for potential field edge detection," *Chin. J. Geophys.-Chin. Ed.*, vol. 65, no. 5, pp. 1785–1801, May 2022.

[43] A. M. Albora, A. Bal, and O. N. Ucan, "A new approach for border detection of the Dumluca (Turkey) iron ore area: Wavelet cellular neural networks," *Pure Appl. Geophys.*, vol. 164, no. 1, pp. 199–215, Jan. 2007.

[44] R. F. Annan and X. Wan, "Recovering bathymetry of the Gulf of Guinea using altimetry-derived gravity field products combined via convolutional neural network," *Surv. Geophys.*, vol. 43, no. 5, pp. 1541–1561, Jul. 2022.

[45] S. Zhao, D. Liu, Q. Yuan, and J. Li, "A global gravity reconstruction method for mercury employing deep convolutional neural network," *Remote Sens.*, vol. 12, no. 14, p. 2293, Jul. 2020.

[46] S. He, H. Cai, S. Liu, J. Xie, and X. Hu, "Recovering 3D basement relief using gravity data through convolutional neural networks," *J. Geophys. Res., Solid Earth*, vol. 126, no. 10, Oct. 2021, Art. no. e2021JB022611.

[47] B. Graham, "Sparse 3D convolutional neural networks," 2015, *arXiv:1505.02890*.

[48] S.-H. Noh, "Performance comparison of CNN models using gradient flow analysis," *Informatics*, vol. 8, no. 3, p. 53, Aug. 2021.

[49] O. Ronneberger, P. Fischer, and T. Brox, "U-Net: Convolutional networks for biomedical image segmentation," in *Proc. Int. Conf. Med. Image Comput. Comput.-Assist. Intervent.*, 2015, pp. 234–241.

[50] Z. Zhang, P. Yu, L. Zhang, C. Zhao, Y. Wang, and Y. Xu, "Application of U-Net for the recognition of regional features in geophysical inversion results," *IEEE Trans. Geosci. Remote Sens.*, vol. 60, 2022, Art. no. 4705207.

[51] L. Zhang and G. Zhang, "3-D gravity inversion based on cross dimensional deep neural networks," in *Proc. 4th Int. Workshop Math. Geophys., Traditional Learn.*, 2021, pp. 166–169.

[52] K. Li et al., "Salt structure identification based on U-Net model with target flip, multiple distillation and self-distillation methods," *Frontiers Earth Sci.*, vol. 10, p. 2387, Jan. 2023.

[53] L. Zhang, G. Zhang, Y. Liu, and Z. Fan, "Deep learning for 3-D inversion of gravity data," *IEEE Trans. Geosci. Remote Sens.*, vol. 60, 2022, Art. no. 5905918.

[54] L. Lou, F. Zhang, and B. Han, "Research on salt dome recognition algorithm based on reverse attention mechanism," *Proc. SPIE*, vol. 12344, pp. 364–368, Oct. 2022.

[55] A. P. O. Müller et al., "Complete identification of complex salt geometries from inaccurate migrated subsurface offset gathers using deep learning," *Geophysics*, vol. 87, no. 6, pp. 453–463, Nov. 2022.

[56] Y. Zhang, Y. Liu, H. Zhang, and H. Xue, "Automatic salt dome detection using U-Net," in *Proc. 81st EAGE Conf. Exhib.*, 2019, pp. 1–5.

[57] S. A. S. Al-Duri and A. H. Abbas, "Seismic images interpretation to discover salt domes using deep fully convolutional network," *J. Phys., Conf.*, vol. 1818, no. 1, Mar. 2021, Art. no. 012006.

[58] A. Motasharreie and H. Zomorrodian, "Modeling of a salt dome structure using the gravity data," in *Proc. 13th EAGE Eur. Meeting Environ. Eng. Geophys.*, 2007, p. 30.

[59] J. Chen et al., "Machine learning method to determine salt structures from gravity data," *Proc. SPIE*, Oct. 2020, Art. no. SPE-201424-MS.

[60] X. Zhou, Z. Chen, Y. Lv, and S. Wang, "3-D gravity intelligent inversion by U-Net network with data augmentation," *IEEE Trans. Geosci. Remote Sens.*, vol. 61, 2023, Art. no. 5902713.

[61] M. Karchevskiy, I. Ashrapov, and L. Kozinkin, "Automatic salt deposits segmentation: A deep learning approach," 2018, *arXiv:1812.01429*.

[62] L. Zhang et al., "Deep learning approach in characterizing salt body on seismic images," in *Proc. SEG Tech. Program Expanded Abstr.*, 2019, pp. 2594–2598.

[63] M. S. Zhdanov, *Inverse Theory and Applications in Geophysics*. Amsterdam, The Netherlands: Elsevier, 2015, p. 799.

[64] A. Dakhia, T. Wang, and H. Lu, "Multi-scale pyramid pooling network for salient object detection," *Neurocomputing*, vol. 333, pp. 211–220, Mar. 2019.

[65] L.-C. Chen, Y. Zhu, G. Papandreou, F. Schroff, and H. Adam, "Encoder–decoder with atrous separable convolution for semantic image segmentation," in *Proc. Eur. Conf. Comput. Vis.*, 2018, pp. 801–818.

[66] J. Zhang and W. Wang, "Retinal vessel segmentation based on U-Net network," in *Proc. 2nd Int. Conf. Consumer Electron. Comput. Eng.*, 2022, pp. 380–383.

[67] D. Li, G. Wen, Y. Kuai, L. Zhu, and F. Porikli, "Robust visual tracking with channel attention and focal loss," *Neurocomputing*, vol. 401, pp. 295–307, Aug. 2020.

[68] H. Zhu et al., "MS-HNN: Multi-scale hierarchical neural network with squeeze and excitation block for neonatal sleep staging using a single-channel EEG," *IEEE Trans. Neural Syst. Rehabil. Eng.*, vol. 31, pp. 2195–2204, 2023.

[69] Q. Hou, L. Zhang, M.-M. Cheng, and J. Feng, "Strip pooling: Rethinking spatial pooling for scene parsing," in *Proc. IEEE/CVF Conf. Comput. Vis. Pattern Recognit.*, Jun. 2020, pp. 4003–4012.

[70] L. Gernigon et al., "Basement inheritance and salt structures in the SE Barents Sea: Insights from new potential field data," *J. Geodynamics*, vol. 119, pp. 82–106, Sep. 2018.

[71] S. Nybakken and R.-A. Berg, "The Nordkapp Basin, Barents Sea—Basin development and halokinesis," in *Proc. 55th EAEG Meeting*, 1993, p. 46.

[72] L. A. Rojo and A. Escalona, "Controls on minibasin infill in the Nordkapp Basin: Evidence of complex Triassic synsedimentary deposition influenced by salt tectonics," *AAPG Bull.*, vol. 102, no. 7, pp. 1239–1272, Jul. 2018.

[73] J. I. Faleide, S. T. Gudlaugsson, and G. Jacquart, "Evolution of the western Barents sea," *Mar. Petroleum Geol.*, vol. 1, no. 2, pp. 123–150, May 1984.

[74] A. G. Doré, "Barents sea geology, petroleum resources and commercial potential," *ARCTIC*, vol. 48, no. 3, pp. 207–221, Jan. 1995.

[75] K. T. Nilsen, B. C. Vendeville, and J.-T. Johansen, *Influence of Regional Tectonics on Halokinesis in the Nordkapp Basin, Barents Sea*. Tulsa, OK, USA: American Association of Petroleum, 1995.

[76] S. Johansen et al., "Hydrocarbon potential in the Barents Sea region: Play distribution and potential," in *Norwegian Petroleum Society Special Publications*. Amsterdam, The Netherlands: Elsevier, 1993, pp. 273–320.

[77] M. S. Zhdanov and W. Lin, "Adaptive multinary inversion of gravity and gravity gradiometry data," *Geophysics*, vol. 82, no. 6, pp. 101–114, Nov. 2017.

[78] Z. Xu, L. Wan, and M. S. Zhdanov, "Focusing iterative migration of gravity gradiometry data acquired in the Nordkapp Basin, Barents Sea," *Geophys. Prospecting*, vol. 68, no. 7, pp. 2292–2306, Sep. 2020.

Rui Wang received the Ph.D. degree in traffic and transportation engineering from Jilin University, Changchun, China, in 2014.

Currently, he is an Associate Professor and the Head of the Software Engineering Department, School of Computer Science and Technology, Changchun University of Science and Technology, Changchun. His main research interests include machine learning, computer vision, geophysics, and deep learning interpretation of continental dynamics.

Yaming Ding received the bachelor's degree in computer science and technology from Yangzhou University, Yangzhou, China, in 2020. He is currently pursuing the master's degree with the Changchun University of Science and Technology, Changchun, China.

His research interests include machine learning and computer vision.

Zhengwei Xu received the M.Sc. degree in geo-exploration science and information technology from Jilin University, Changchun, China, in 2008, and the Ph.D. degree in geophysics from The University of Utah, Salt Lake City, UT, USA, in 2013.

He is currently a Researcher with the College of Geophysics, Chengdu University of Technology, Chengdu, China. His research interests include gravity, magnetic, and electromagnetic forward modeling and inversion theory, as well as incorporation and joint inversion of multigeophysical data using artificial intelligence.

Yu Zhang received the B.S. degree in geophysics from the Chengdu University of Technology, Chengdu, China, in 2023, where he is currently pursuing the Ph.D. degree.

His research interests include gravity and magnetic inversion imaging.

Michael S. Zhdanov (Member, IEEE) received the M.Sc. degree in geophysics from the Moscow Gubkin State University of Oil and Gas, Moscow, Russia, in 1970, and the Ph.D. degree in physics and mathematics from Moscow State University, Moscow, in 1978.

He is currently a Distinguished Professor with the Department of Geology and Geophysics, The University of Utah, Salt Lake City, UT, USA, the Director of the Consortium for Electromagnetic Modeling and Inversion (CEMI), and the CEO and the Chairperson of TechnoImaging, Salt Lake City. He is also an Honorary Gauss Professor of the Göttingen Academy of Sciences, Göttingen, Germany, and an Honorary Professor of the China National Centre for Geological Exploration Technology, Beijing, China. His research interests include fundamental and applied geophysics, inversion theory, electromagnetic theory, methods, and integration and joint inversion of multiphysics data.

Dr. Zhdanov is a fellow of the Russian Academy of Natural Sciences and Electromagnetics Academy USA, and an Honorary Member of the Society of Exploration Geophysicists.
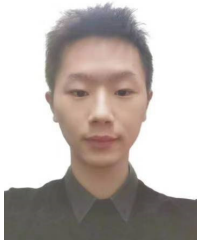
Jun Li received the B.S., M.Sc., and Ph.D. degrees in geophysics from the Chengdu University of Technology, Chengdu, China, in 2001, 2005, and 2010, respectively.

His research interests include fundamental and applied geophysics, inversion theory, gravity, and magnetic theory and methods.

Chao Jiang received the bachelor's degree in internet of things engineering from Heze University, Heze, China, in 2021. He is currently pursuing the master's degree with the Changchun University of Science and Technology, Changchun, China.

His research interests include machine learning and computer vision.

Minghao Xian received the B.S. degree in geophysics from the Chengdu University of Technology, Chengdu, China, in 2023, where he is currently pursuing the M.S. degree.

His research interests include gravity and magnetic inversion imaging.

Ziqing Guo is currently pursuing the B.S. degree with the Chengdu University of Technology, Chengdu, China.

Her research interests include gravity and magnetic inversion imaging.